Magnetic and Optical Characterisation of the Layered Van der Waals Antiferromagnet CrSBr

Vera Kok

Chemistry/Chemical Physics 5P Thesis

Supervisors: Jorik van de Groep (UvA), Sander Mann (UvA), Anna Isaeva (UvA), Iain Wright (UoE)

Date: 11th June 2026

Combined Word Count: 6948

Confidentiality

The contents of this report have been approved by the supervisors running this project and I declare the work as a non-confidential project (report available to exam moderators/external examiners)

Declaration

I declare that this thesis was composed by myself, that the work contained herein is my own except where explicitly stated otherwise in the text, and that this work has not been submitted for any other degree or qualification.

Acknowledgements

I would like to thank Jorik van de Groep, Sander Mann and Anna Isaeva (my supervisors at the University of Amsterdam) for giving me this amazing opportunity to see what working in academia is like. I thoroughly enjoyed my experience and am very grateful to how openly I was welcomed into all three research groups. I believe their accepting nature made it much easier for me to try my hand as a complete beginner in a laser lab.

I would like to thank Stephanie, Wouter, Umut and Rein for forming the foundation of my time at the UvA. Having a space to go to with people I slowly grew closer to during the project was a blessing. We were very good at distracting each other and having a good old yap and giggle- especially Stephanie and I (sorry everyone else in the masters room). It was devastating when we lost the masters room and I didn't get to see you all as often.

Thank you to Alvaro for your endless time to explain things and helping me set things up (so well might I add), Bernardo for training me on the WITec (the first scary instrument I got to use) and Tom for teaching me how to exfoliate crystals (step one of the project). Thank you to Mehmet for dedicating a good few days to sitting in a dark room taking measurements with me and thank you to Eva, Anne, David (for facilitating my new monitor addiction), Freek, Ershad and Reynolds for being so welcoming and making me feel at home at the UvA.

Thank you to Sander's research group for tolerating my fleeting appearances but always making me feel welcome, I really enjoyed the group outings. Thank you to Charly for inviting me to help organise a conference, a learning experience I will no doubt reap the benefits from for years to come.

Another thank you to Anna's research group- again the group outings were great. It was such a nice introduction to the university when I met Laura a few months earlier for a lab tour. Thank you to Grisha for the first few trainings and always being there to answer questions. I am grateful to Javier for immediately making an effort to get to know me and making me feel grounded from the second week. I really enjoyed my NWO experience with Auguste, Laura and Marie and from then onwards I loved all the giggles we could share in the hallways.

Thank you to Laura C and Anne de Visser for all the time you generously gave to me to help me set-up and understand measurements with the PPMS.

Thank you to mum and dad for helping me through the year abroad when I wasn't feeling it. Your constant support is overwhelming and I am so grateful. Thank you to all the friends (Amrit, Amaia, Jane, Harry and Sophie) that came to visit me and remind me of the big wide world outside of university-

your visits helped me through the months!

Also a shout-out to my 7 year-old laptop that managed so well for the whole year. Expectations were low in the first month but look at all the apps I managed to download and still run!!!

And last but by no means least, thank you to my lovely boyfriend Jonny. We did it! We managed long distance (easy peasy actually, lets do it again? ;)). I am forever grateful to your ability to say all the right things. You are my rock.

Abstract

Two-dimensional van der Waals materials have emerged as promising candidates for next-generation optoelectronic technologies due to their tunable electronic and optical properties. In particular, materials that exhibit strong coupling between magnetic and optical behaviours offer opportunities for dynamic control in applications such as tunable metasurfaces. Chromium sulphide bromide (CrSBr) is one such material, combining semiconducting properties with antiferromagnetic order. This project experimentally characterises the magnetic and optical properties of commercially sourced CrSBr crystals and assesses their consistency with current literature alongside investigating the coupling between these two properties.

Magnetic behaviour was investigated using AC and DC magnetic susceptibility measurements. The results confirm strong triaxial magnetic anisotropy and A-type antiferromagnetic ordering below a Néel temperature of 132.7(6) K. Field-dependent measurements reveal distinct spin-flip and spin-reorientation mechanisms along different crystallographic axes with saturation moments consistent with the expected spin-only value. In addition to the primary magnetic transition, a secondary feature near 39 K was observed. Its dependence on applied magnetic field and excitation frequency suggests the presence of slow magnetic dynamics, consistent with a spin-glass-like or frustrated magnetic phase.

Optical properties were probed using photoluminescence spectroscopy. A dominant excitonic emission near 1.31 eV was observed at room temperature, while low temperature measurements reveal a splitting of this peak that collapses at the Néel temperature. This behaviour provides clear evidence of coupling between magnetic ordering and excitonic states. Conversely, no change was observed in the photoluminescence spectra with no applied magnetic field around 39 K.

Overall, the results validate the expected properties of CrSBr while revealing additional low-temperature magnetic complexity, supporting its potential for tunable nanophotonic and optoelectronic applications.

Abbreviations

- AFM: Antiferromagnetic
- FM: Ferromagnetic
- PM: Paramagnetic
- AC: Alternating Current
- DC: Direct Current
- ZFC: Zero Field Cooled
- FC: Field Cooled
- FWHM: Full Width Half Maximum
- PL: Photoluminescence
- vdW: van der Waals

Contents

1 Project Background and Objectives

Technological advancements and the demand for compact, energy-efficient devices are driving a transition from traditional bulk three-dimensional (3D) materials to atomically thin two-dimensional (2D) materials. Composed of layers only a few atoms thick, these materials exhibit properties that differ significantly from their bulk counterparts[1] due to quantum confinement and reduced dimensionality. Since the isolation of graphene in 2004[2] , research into 2D materials has expanded rapidly, revealing a diverse class of so-called van der Waals materials- layered systems held together by weak interlayer van der Waals forces.

One promising application of 2D materials is in metasurfaces, which are engineered planar structures designed to manipulate electromagnetic waves. Unlike conventional optical components that rely on bulk material properties, metasurfaces achieve control over light through subwavelength structuring[3], enabling ultra-thin devices capable of focusing, filtering, or modulating light. However, most metasurfaces developed to date are static, with properties that are fixed after fabrication. A key challenge in the field is therefore the development of dynamic metasurfaces that can be tuned in real time in response to external stimuli such as electric fields, strain, or magnetic fields.

Quantum materials (materials whose macroscopic properties require quantum mechanical descriptions) offer a potential solution to this challenge. These materials exhibit strongly coupled electronic, optical, and magnetic properties, meaning that a change in one property can influence others. This coupling enables external control over optical response, which is highly desirable for tunable photonic devices[4]- with applications in beam steering, tunable optical filters, optical modulators and smart lenses.

A particularly promising material in this context is chromium sulphide bromide (CrSBr), a layered van der Waals material that exhibits both semiconducting *and* antiferromagnet behaviour. A semiconductor is defined by a fully occupied valence band and an empty conduction band at a temperature of absolute zero (0 K) with electrical conductivity arising from the promotion of electrons to the conduction band through external stimuli such as temperature, light, or doping. The resulting electrons and holes can form electrostatically bound states known as excitons which play a central role in the optical properties of semiconductors. When excitons recombine, photons can be emitted, providing a characteristic signature observable in photoluminescence spectroscopy.

In particular, when the energy of incident light matches that required to form an exciton- referred to as excitonic resonance- the optical response of CrSBr is strongly enhanced. Near this resonance, the refractive index of CrSBr becomes very large[4] and highly sensitive to external perturbations. As a consequence, parameters such as strain[5,6] and electrical gating[7] can significantly modify the refractive

index in the spectral range around exciton resonance.

An antiferromagnet is a magnetic material in which neighbouring spins align in opposite directions resulting in a zero net magnetisation[8]. In CrSBr, the coexistence of semiconducting properties and magnetic order provides the opportunity for a uniquely strong coupling between optical and magnetic properties. As a result, changes in magnetic ordering can directly influence the material's interaction with light[9]. Such magnetically driven control of optical properties is rare in conventional materials, highlighting the significance of CrSBr for tunable photonic applications. This combination of properties makes it particularly attractive for the development of magnetically controlled dynamic metasurfaces.

In addition to its functional properties, CrSBr is experimentally accessible. It is stable under ambient conditions[10] and can be easily mechanically exfoliated (or separated) into thin layers[11], facilitating its integration into devices and heterostructures (materials engineered by joining two or more thin layers of semiconductor materials). These characteristics make it suitable not only for fundamental research but also for potential technological applications such as in autonomous systems, consumer electronics, telecommunications and sensing in healthcare applications.

1.1 Project Aims and Objectives

While CrSBr has shown promise for tunable optoelectronic applications, inconsistencies in reported low-temperature magnetic behaviours and variability between samples present a major challenge for both fundamental understanding and technological implementation. In particular, some sources see a secondary peak in magnetic susceptibility around 39 K[8,12–14] whilst others do not[15]. Reliable device performance depends critically on well-defined and reproducible material properties. As a result, resolving these discrepancies and establishing consistent behaviour is an essential step towards the practical use of CrSBr in functional devices. As the CrSBr crystals used in this project were sourced externally (HQ Graphene) and had not been previously characterised within the Institute of Physics at the University of Amsterdam, their properties required verification.

The primary aim of this project was therefore to **experimentally characterise the magnetic and optical properties of CrSBr samples, examine the reported coupling between these degrees of freedom, and evaluate their consistency with literature**. These objectives were pursued through a combination of complimentary experimental techniques. The magnetic phase diagram was determined by measuring the magnetic susceptibility as a function of temperature, applied magnetic field, and crystallographic orientation. This provided insight into the magnetic ordering of the material. Temperature-dependent photoluminescence spectroscopy was used to characterise the optical response

of the material and investigate excitonic behaviour as a function of magnetic ordering. The results were then compared with previously reported results to evaluate reproducibility and identify any discrepancies.

These objectives are important not only for validating the quality of the material but also for addressing key uncertainties in the current literature. Establishing reproducible magnetic and optical behaviour is essential for both advancing the fundamental understanding of CrSBr and enabling its reliable integration into tunable nanophotonic devices. More broadly, this work contributes to the development of low-dimensional quantum materials for next-generation optoelectronic technologies, where precise control over coupled physical properties is crucial.

2 Results and Discussion

2.1 Background Theory and Information

In order to contextualise the results given in this thesis, it is helpful to understand the crystal structure of CrSBr and the chief magnetic exchange interactions that bring about the so-called A type antiferromagnetic order.

2.1.1 Crystal Structure of CrSBr

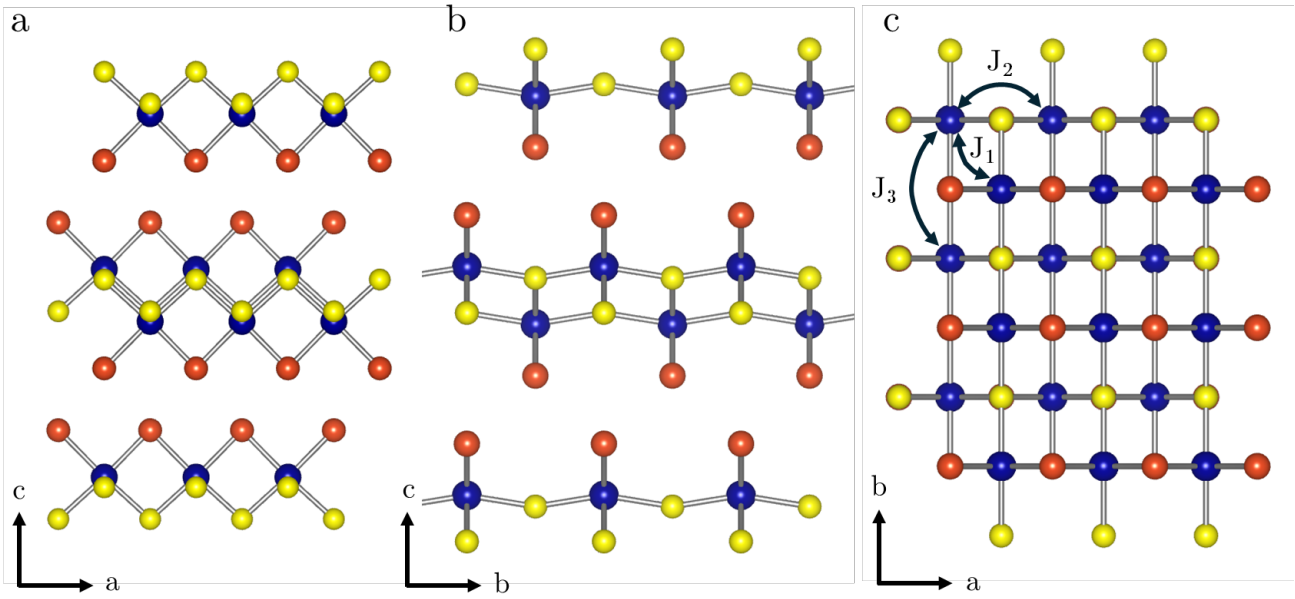

Figure 1: *(a–c) Crystal structures of CrSBr viewed within the ac (a), bc (b), and ab (c) planes. Blue, yellow, and red spheres correspond to Cr, S, and Br atoms, respectively. In (c), arrows indicate the three nearest neighbour exchange pathways. Figure reproduced from Ziebel* et al. [10]

CrSBr crystallises in the FeOCl structure type with the orthorhombic space group *Pmmn* and unit cell parameters $a = 3.506(2)$ Å, $b = 4.767(2)$ Å and $c = 7.965(4)$ Å [16]. The crystal structure consists of buckled chromium sulphide double layers capped on both sides by an anionic bromide layer and separated by a van der Waals gap along the *c*-axis (**Figure 1 (a) and (b)**). Along the *a*-axis, chromium ions are bridged by sulphide and bromide ions with Cr–S–Cr and Cr–Br–Cr bond angles near 90°; along the *b*-axis, chromium ions are bridged by sulphide ions with a Cr–S–Cr bond angle of 162° (**Figure 1 (c)**). This in-plane bonding anisotropy causes crystals to grow as rectangular plates elongated along the crystallographic *a*-axis (**Figure 2**) which allows simple visual assignment of the crystallographic axes of a sample.

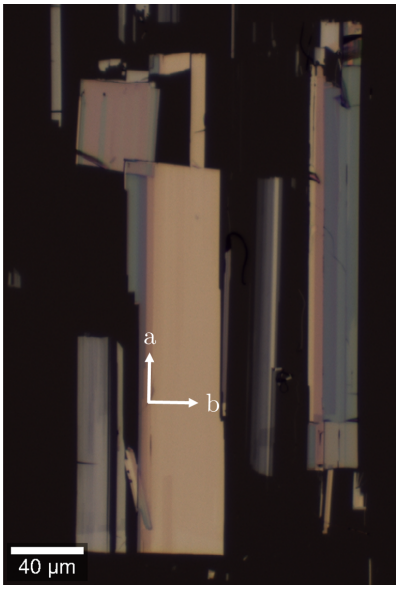

Figure 2: *Optical micrograph of mechanically exfoliated CrSBr viewed within the ab plane. Exfoliation results in needle-like crystal plates of differing thickness with the a crystallographic axis extending along the long edge of the needles. Crystal thickness is dependent on how many layers of material are left behind after exfoliation and higher contrast with the background indicates thicker crystal sections. Multiple crystal fragments are depicted Scale bar:* $40\mu m$.

2.1.2 Magnetic Exchange Interactions

The magnetic properties of CrSBr arise from Cr(III) ions with 3 unpaired spins, resulting in a $S = \frac{3}{2}$ state. Neighbouring magnetic Cr^{3+} ions interact and how they interact is dictated by the quantum mechanical exchange energy, which describes the energy difference between parallel and antiparallel spin alignments. The crystal structure of CrSBr then dictates that the strongest magnetic interactions are the nearest-neighbour superexchange pathways labelled J_1 through J_3 in **Figure 1 (c)**, facilitated by the overlap of half-filled Cr^{3+} orbitals with filled orbitals on intermediate S^{2-} and Br^{-} anions.

According to the Goodenough-Kanamori[17] rules, the cation-anion-cation angles extracted from neutron diffraction data[12] imply ferromagnetic coupling for J_1 and J_2, and competing ferromagnetic and antiferromagnetic interactions for J_3. Interlayer exchange between vdW layers ($|J_{IL}|$) is much weaker due to poor orbital overlap within Cr-Br-Br-Cr linkages, indicating antiferromagnetic exchange may dominate here. Indeed, inelastic neutron scattering (INS) measurements reveal that all three intralayer super exchange pathways are ferromagnetic with $|J_2| > |J_1| > |J_3|$ and $|J_{IL}|$ is 2 to 3 orders of magnitude lower than $|J_2|$[18]. **Table 1** summarises the findings for the magnetic exchange interactions where negative exchange energies correspond to ferromagnetic exchange interactions.

Table 1: *Summary of chemical linkages, cation-anion-cation angles and the exchange energies for the three strongest super-exchange interactions in CrSBr. Data taken from*[18] *and presentation taken from*[10].

	Bridging Anion	Bond Angle (deg)	Exchange Energy (meV)
J_1	S, Br	94.0 (S) 89.4 (Br)	-1.90
J_2	S	94.6	-3.38
J_3	S	161.6	-1.67

As indicated by the above exchange interactions, CrSBr exhibits **A-type antiferromagnetic order**: spins are ferromagnetically aligned within layers and antiferromagnetically between layers, see **Figure 3**[19,20]. The onset of antiferromagnetic ordering occurs below 132 K (the Néel temperature T_N)[8,9,12,18,19,21–23].

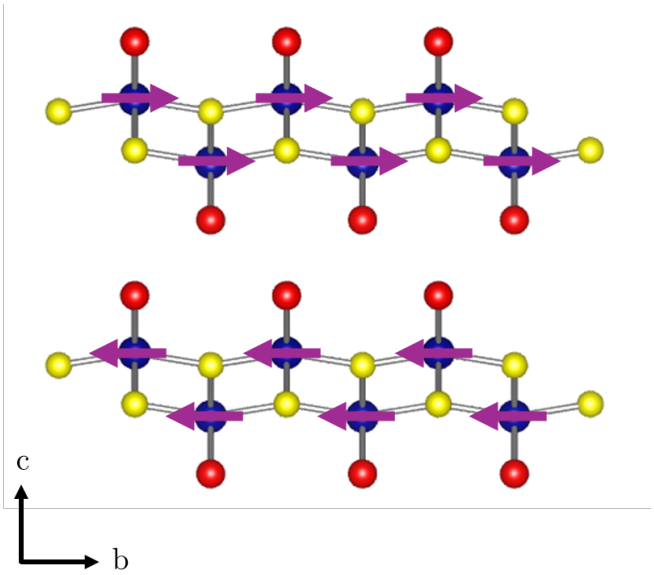

Figure 3: *Schematic showing two layers of CrSBr stacked along the* c*-axis viewed along the* a*-axis. The paramagnetic spins (purple arrows) from the Cr ions align ferromagnetically within each layer but align antiferromagnetically between layers.*

2.2 Magnetic Characterisation

Characterisation of the magnetic phase diagram of the CrSBr samples was performed via magnetic susceptibility measurements using a Quantum Design Physical Property Measurement System (PPMS) equipped with the ACMS II Measurement Option. Magnetic susceptibility measurements probe how a material responds to an applied magnetic field and in this project two distinct methods were used; namely alternating current (AC) and direct current (DC) magnetic susceptibility.

In DC measurements, a constant magnetic field is applied, providing information about the equilibrium magnetic response of the system. In contrast, AC susceptibility applies a small oscillating field (sometimes in addition to a DC field), allowing the material response to be separated into a real component (χ'), representing reversible magnetisation, and an imaginary component (χ"), which is associated with energy dissipation and dynamic processes within the material.

In this project, AC and DC magnetic susceptibility was measured as a function of temperature and external field strength. Due to the triaxial anisotropy of CrSBr, all investigations were performed along all three crystallographic axes.

2.2.1 Magnetic Susceptibility as a Function of Applied Magnetic Field

A standard initial magnetic characterisation method is the measurement of the magnetic susceptibility with varying field. **Figure 4** shows the strong triaxial magnetic anisotropy present in the CrSBr crystals. Without an external magnetic field, the crystal is in the antiferromagnetic ground state at 2 K. The application of a magnetic field of increasing magnitude along the 3 different axes eventually attains a field-polarised ferromagnetic state with the same saturation moment of 2.9 μ_B for each axis (the expected spin-only saturation moment from Cr^{3+} ions is 3 μ_B). However, the pathway towards saturation differs per crystallographic axis. Firstly, saturation is achieved at 0.56 T, 1.03 T and 1.99 T for the *b*, *a* and *c* crystallographic directions, respectively. This qualifies the *b*-, *a*- and *c*-axes as the easy, intermediate and hard magnetic axes, terms that refer to how easily the spins reorientate to the external field direction with a greater saturation field magnitude indicating that the spins are 'harder' to align.

In addition, whilst the reorientation of spins and hence the increase in magnetic moment is gradual along the *a*- and *c*-axis, the increase is much sharper along the *b*-axis. In this case, the magnetic moment per formula unit of CrSBr remains near-zero until a sharp transition occurs at 0.30 T (known as H_{flip}) and the magnetic moment per formula unit rises quickly to the saturation moment. The feature observed along the *b*-axis is known as a spin-flip transition: the spins are either antiparallel or parallel

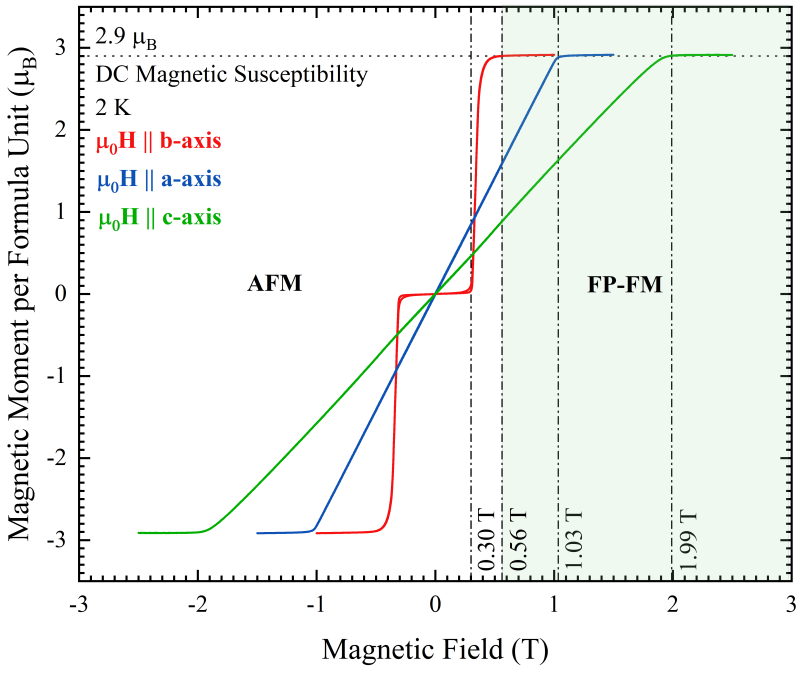

Figure 4: *The magnetic susceptibility of CrSBr along the 3 different crystallographic axes at 2 K with varying magnetic field ranging between -2.5 and +2.5 T. At 2 K, the system is in its AFM ground state and the external magnetic field forces field-polarised ferromagnetic (FP-FM) alignment along the applied field direction. Due to the anisotropy of the system, this occurs at 3 different fields. A sharp increase is seen at 0.30 T along the b direction which signifies a spin-flip transition whilst a gradual reorientation of the spins is seen along the a and c axes. Saturation magnetisation occurs at approximately 0.56, 1.03 and 1.99 T for the* b, a *and* c *axes, respectively. The saturation moment per formula units is shown to be 2.9* μ_B*. The response is symmetric for a field applied in the negative direction, as indicated in the left half of the figure.*

with the field- no intermediate states exist. This is because the spins have a preferred orientation along the *b*-axis when in the antiferromagnetic ground state and maintain this until the field is strong enough to overcome it.

The trends seen in **Figure 4** are consistent with the observations seen by other groups[12,20,24] and present the distinctive triaxial anisotropy of this material.

2.2.2 Magnetic Susceptibility as a Function of Temperature

In order to measure the magnetic response of the CrSBr samples used in this report, it was decided to first use the AC magnetic susceptibility measurement method as the samples were small and the more sensitive method would ensure that observations were possible. The AC magnetic susceptibility as a function of temperature is plotted in **Figure 5**. Such measurements shed light on magnetic transitions types and the corresponding characteristic temperatures. **Figure 5** shows the expected[16,19,20] sharp cusp in real magnetic susceptibility (χ') at 132.7(6) K, indicating a transition from a paramagnetic to antiferromagnetic state (also known as the Néel temperature T_N).

In the high temperature regime, thermal fluctuations dominate and the spins remain largely disordered. As the temperature is reduced towards the Néel temperature, exchange interactions increasingly align the spins, leading to a rise in magnetic susceptibility. At the transition temperature, long-range antiferromagnetic order is established, resulting in a decrease in susceptibility as the magnetic moments align antiparallel.

Along the *b*-axis- corresponding to the easy axis of the antiferromagnetic ground state- the magnetic susceptibility drops to zero below the transition temperature. This occurs because the applied field (0.4 mT) is far smaller than the spin-flip field (300 mT) identified in **Figure 4** and is therefore insufficient to reorient the spins. In contrast, along the *a*- and *c*-axes a finite susceptibility is observed as the applied field can induce partial spin canting and the spins are not perfectly aligned antiparallel. Logically, the magnetic hard axis exhibits a weaker low-temperature response than the intermediate axis in the small AC field. The maximum susceptibility is larger for the *a*- and *b*-axes than for the *c*-axis, reflecting the fact that the spins preferentially lie in the *ab* plane and so respond more to fields applied within the plane than out of plane.

AC magnetic susceptibility measurements along the *a*- and *c*-axis also show a small secondary peak in the imaginary and real component at 38.7(6) K. A peak in the imaginary susceptibility is indicative of dissipative processes. Interestingly, this feature is not visible along the *b*-axis which may be as the spins are more confined along the *b*-axis. However, this observation is inconsistent with literature[8,12,25] where a peak is seen along all crystallographic directions. In fact, López-Paz et al[12] in particular see this feature along all axes using SQUID magnetometry, a more sensitive technique, thus indicating that such features could be beyond the resolution limits of the equipment used. Also important to note is that the slightly heightened background imaginary magnetic susceptibility seen in for the *c*-axis is most likely a measurement issue and unphysical, as the background imaginary susceptibility should be zero in most cases.

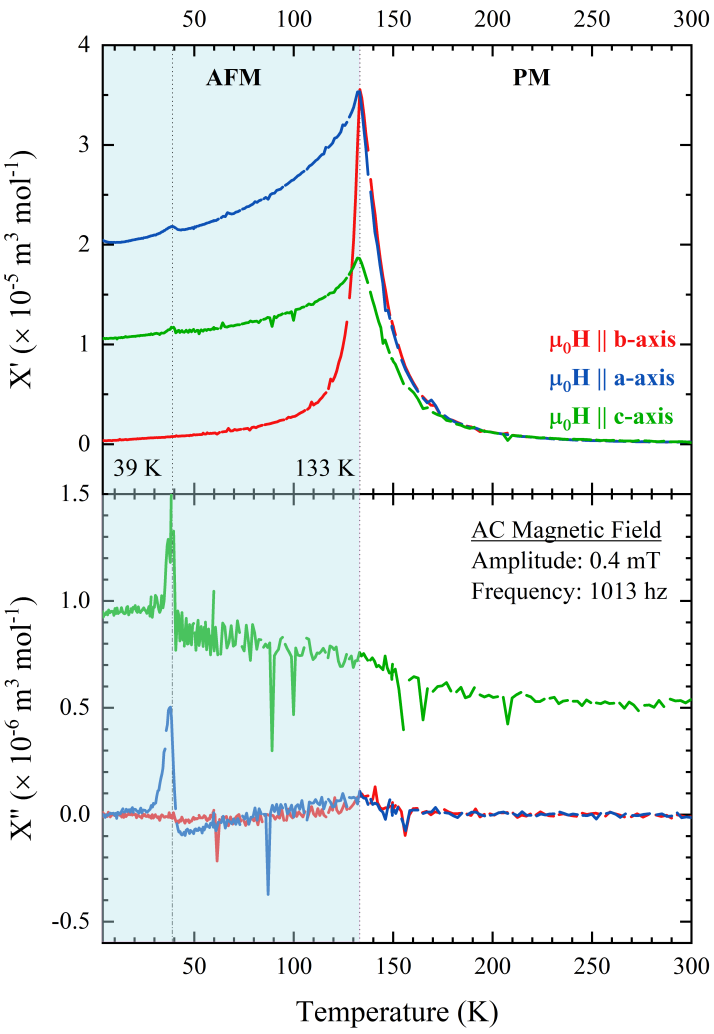

Figure 5: *The temperature dependent real (χ') and imaginary (χ") magnetic susceptibility measured between 300 and 4 K along the three crystallographic axes. A fixed external AC magnetic field with an amplitude of 0.4 mT and frequency of 1013 hz was applied. A sharp cusp in χ' at 133 K along all 3 crystallographic directions is characteristic of an antiferromagnetic transition from the disordered paramagnetic (PM) ground state at high temperature to the ordered antiferromagnetic (AFM) state at lower temperatures. The blue shading indicates the onset of AFM ordering. A smaller peak is observed at 39 K in both χ' and χ" for the* a- *and* c-*axes but is notably absent from measurements along the* b-*axis.*

Figure 6 shows the same experiment as in **Figure 5** , but now using the direct current (DC) magnetic susceptibility measurement process. Although this is a less sensitive method, it is useful to ascertain more about the low temperature peak (if it is visible) and to compare the magnetic susceptibility between zero field cooled (ZFC) and field cooled (FC) measurements. A zero field cooled measurement entails cooling the system without an external field to then measure the susceptibility with an external field on heating, whereas a field cooled measurement involved cooling in an external field before measuring the susceptibility on warming.

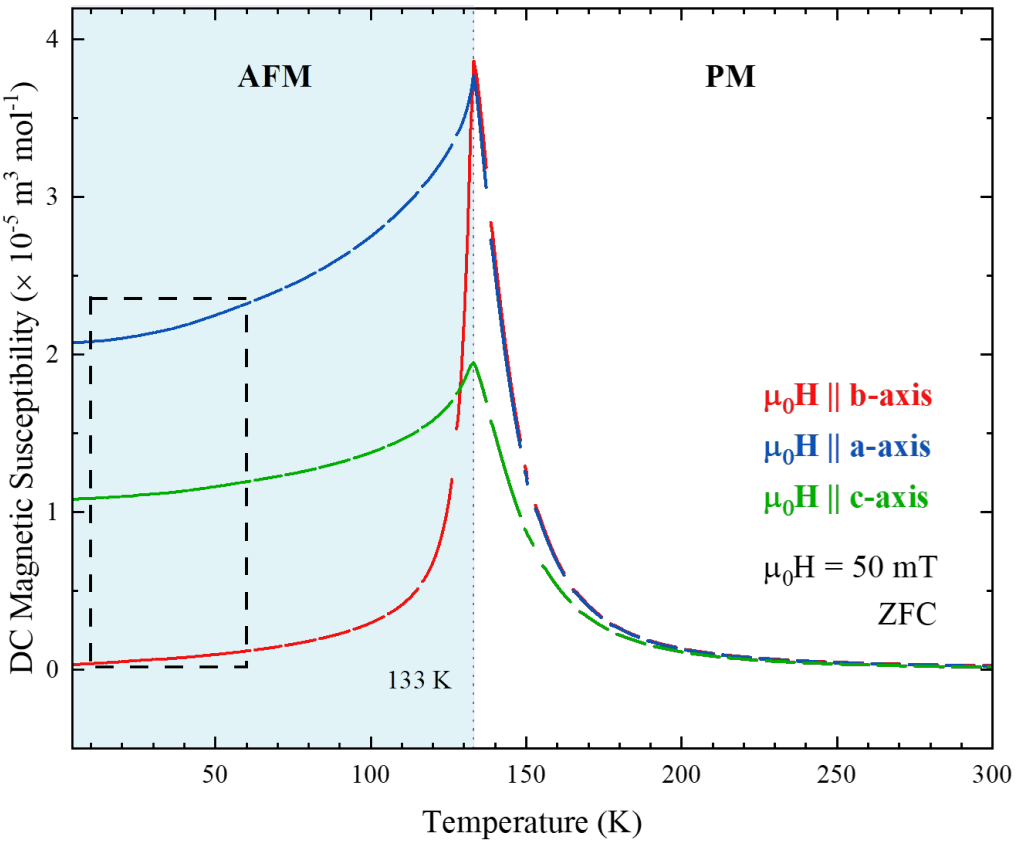

Figure 6: *Comparison of the DC magnetic susceptibility with temperature along the 3 crystallographic axes. At temperatures below the Néel temperature at 133 K, the system is found in the antiferromagnetic (AFM) state whereas at temperature above, the system is found in the paramagnetic (PM) state. The measurements were taken whilst warming in a field of 50 mT after cooling without field, known as a zero field cooling (ZFC) measurement. The area in the dotted box indicates the region inspected in* ***Figure 7****.*

The results show a similar trend to the AC magnetic susceptibility results, except that it seems the low temperature peak is no longer visible. The gaps in the data set are due to measurement settings and have no physical meaning.

DC measurements also allow further analysis of the paramagnetic regime of the material- namely, through processing the data according to the Curie-Weiss law. By fitting the inverse magnetic susceptibility (χ^{-1}) as a function of temperature (T) with the linearised Curie-Weiss law (**Equation 1**), one can extract the Curie constant (C) and Curie-Weiss temperature (θ_{CW}) which contain information about the effective magnetic moment (μ_{eff}) and the strength of the molecular field and magnetic correlations respectively. The extracted linear fit values are shown in **Table 2**.

$$\chi^{-1} = \frac{T}{C} - \frac{\theta_{CW}}{C} \tag{1}$$

Table 2: *Extracted fit parameters for Curie-Weiss fitting of the paramagnetic regime of DC magnetic susceptibility data in* ***Figure 6****.*

Crystallographic Axis	C (emu K mol^{-1} Oe^{-1})	C ($\times 10^{-5}$ m^3 K mol^{-1})	μ_{eff} (μ_B)	Θ_{CW} (K)
b	2.39(2)	3.00(2)	4.37(2)	188(3)
a	2.00(15)	2.51(2)	4.00(15)	195(2)
c	0.98(13)	1.23(17)	2.80(2)	224(5)

The fits for Curie-Weiss analysis were tenuous, varying greatly per data range included and for this reason further analysis including a temperature independent term was not indulged. Another factor leading to poor Curie-Weiss fitting is the small range of temperatures in the dataset above the Néel temperature- relative to other magnetic materials with much lower transition temperatures. The available linear range was even smaller for the *c*-axis which may explain why it differs to such an extent from the extracted parameters for the *b*- and *a*-axis. Despite this, the effective moments (μ_{eff}) extracted from the fits do agree to an extent with the expected calculated spin-only moment of 3.87 μ_B. In addition, the extracted Curie-Weiss temperatures are largely consistent between the measurements along the different crystallographic axes. A positive Θ_{CW} value greater than T_N, signifies that strong local ferromagnetic interactions persist in the crystal above T_N, an observation also made by Telford et al[8]. Single crystal neutron diffraction results from Scheie et al[18] provide evidence that magnetic correlations in the *ab*-plane do indeed persist above T_N.

However, upon close inspection and comparison of DC measurements in zero field cooling (ZFC) and field cooling (FC) settings (**Figure 7**), a subtle splitting along the *b*- and *c*-axes is observed where the low-temperature feature had been seen in **Figure 5**. This splitting is indicative of hysteresis behaviour, which suggests that there are some magnetic domains embedded within the long range antiferromagnetic ordering that are showing ferromagnetic-like behaviour and that are not aligned with the overall long-range ordering.

A lack of distinctive feature for the *a*-axis at approximately 39 K is inconsistent with results seen in literature by other groups[8,12,13] that observe the splitting along all three crystallographic directions. However, the splitting for the *a*-axis in these publications is the smallest and it may then be that sample size and measurement sensitivity may have limited observations in this direction for the measurements made in this report. Reproducible results need to be made to draw any meaningful conclusions.

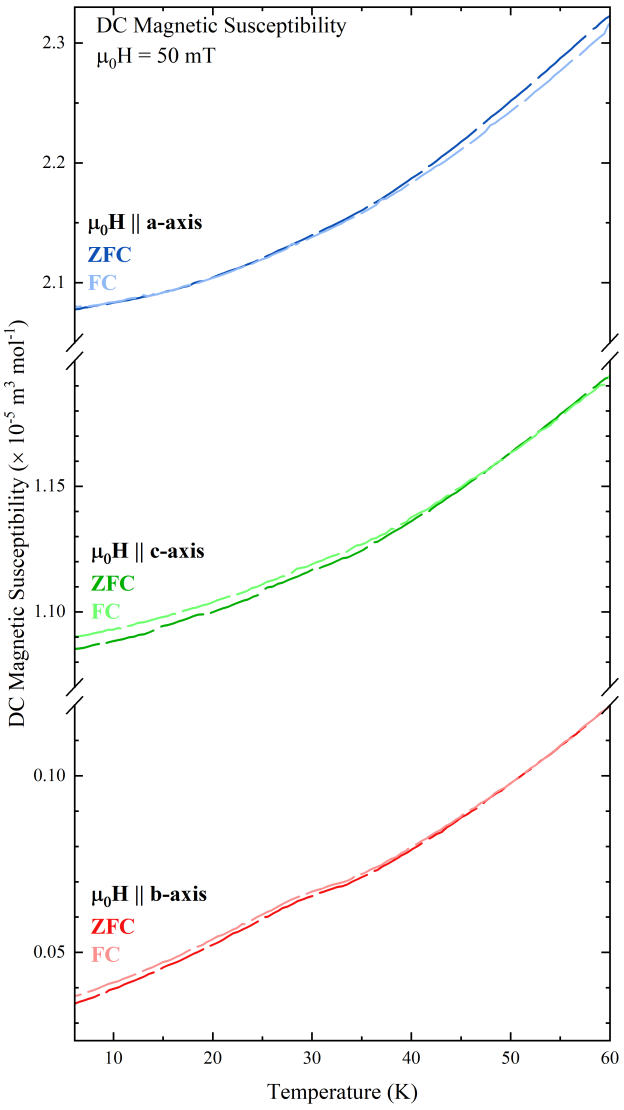

Figure 7: *A plot showing the difference between zero field cooled (ZFC) and field cooled (FC) magnetic susceptibility curves with temperature along the 3 crystallographic axes between 5 and 60 K. A subtle splitting at 30-40 K is seen along the* b- *and* c-*axis whilst this feature is missing along the a-axis measurements.*

2.2.3 Investigation of the Low Temperature Magnetic Susceptibility Feature

To further investigate this low temperature peak and to understand the effect of the external field on this feature, a DC field of varying strength was now applied whilst measuring the AC magnetic susceptibility (**Figure 8**). This was also performed in order to understand if the low temperature peak in magnetic susceptibility became less visible in DC measurements at 50 mT due to measurement sensitivity or field suppression.

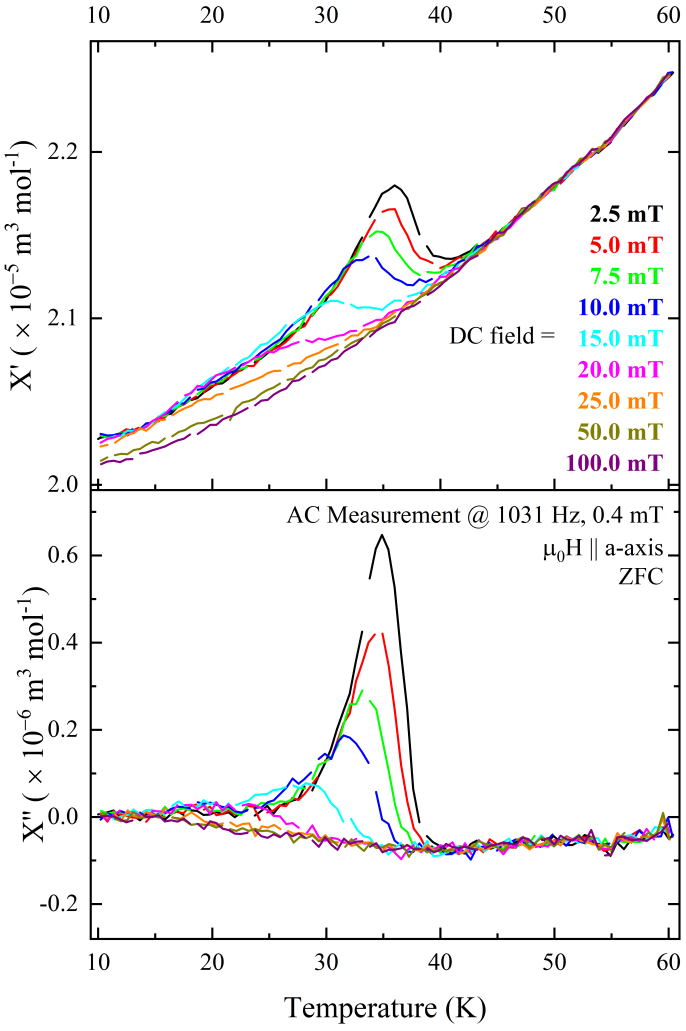

Figure 8: *The real (χ') and imaginary (χ") AC magnetic susceptibility at low temperature with an applied DC magnetic field of increasing strength. A clear reduction in peak magnitude is seen with increasing DC field strength. The measurements were taken with the magnetic fields along the* a*-axis under zero field cooled (ZFC) conditions. The AC field had an amplitude of 0.4 mT and frequency of 1031 Hz.*

It was observed in **Figure 8** that the peak in both the real and imaginary susceptibility at approx-

imately 39 K reduces in magnitude with increasing DC field strength, becoming largely undetectable at 25 mT. Alongside this, the peak shifts to lower temperatures with increasing DC field. Therefore, this data set very clearly suggests that, under AC measurement conditions, the mechanism behind the peak at 30-40 K is suppressed by an increasing DC field. Alongside the observed shift towards lower temperatures this suggest that the system that causes this low temperature feature is becoming less energetically stable as the DC field increases and is more likely to conform to the long-range magnetic ordering. This suppression may also partly explain why the peak is not visible in the aforementioned DC experiments as the DC field used was 50 mT.

The imaginary AC magnetic susceptibility response measured in **Figure 5** indicates that the phase responsible for the low temperature peak is responsive to an oscillatory field. To test if this peak is a dynamic or static feature, its dependence on AC measurement frequency was also studied (**Figure 9**).

Increasing the excitation frequency seems to suppress the peak in real magnetic susceptibility at low temperature. In addition, the peak seems to shift to slightly higher temperatures with higher frequencies. The observed frequency dependence suggests that the magnetic system responsible for the peak is spin-glass-like with slow dynamics. A spin glass entails a dilute random distribution of magnetic atoms with mixed interactions, characterised by a random, yet cooperative freezing of the spins at a well defined temperature below which a metastable state appears without the usual magnetic long-range ordering. In this case the freezing temperature may be 39 K. Spin glass domains often interact weakly, which may explain why increasing the field strength suppresses the peak (as seen in **Figure 8**) as the field is able to force total long-range antiferromagnetic order.

The imaginary magnetic susceptibility peak shows no real change aside from increased resolution which can be explained by increased equipment sensitivity at higher frequencies. Again, the increasing baseline offset is most likely unphysical and an artifact whose origin was not confirmed.

Several papers have suggested separate origins of this low temperature feature. Song et al[14] suggest that the susceptibility kink is the ferromagnetic signature of a $CrBr_3$ secondary phase caused by the annealing of CrSBr crystals near its critical decomposition temperature. However, the observed peak shifts with frequency and field would not be expected from a ferromagnetic phase transition. This phase was also not visible in the microscope as is suggested. Telford et al[8] suggest self-trapped electrons near donor sites as the defect responsible for the feature whereas López-Paz et al[12] suggest a spin freezing process into a frustrated magnetic state. These results could align with either of those theories.

Overall, the trends for the peak shown in **Figures 8** and **9** are indicative of slow magnetic dynamics, such as a spin glass or frustrated magnetic system. Most likely the system undergoes a magnetic freezing or glassy transition around 35-40 K.

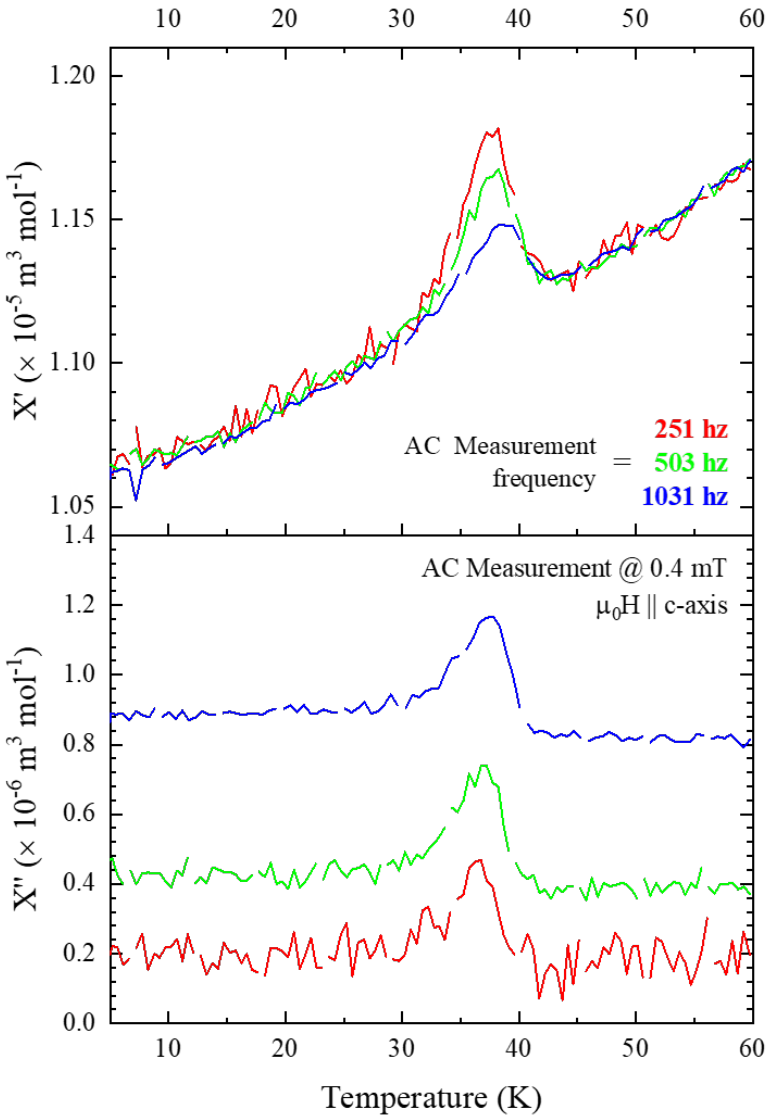

Figure 9: *The real (χ') and imaginary (χ") AC magnetic susceptibility with temperature at different excitation frequencies. The magnetic fields were applied along the* c*-axis and the magnitude of the AC field was 0.4 mT. Increasing frequency appears to decrease the magnitude of the peak in real magnetic susceptibility.*

2.3 Optical Characterisation

As mentioned in **Section 1**, the optical properties of CrSbr provide insight into the electronic structure and exciton energies of the material. Due to the coupling between magnetic and electronic degrees of freedom in CrSBr, the optical properties have the additional ability to provide information about the magnetic state of the material and for these reasons the optical properties of CrSBr were studied.

The electronic structure of CrSBr is characterised by pronounced anisotropy and the presence of high-energy excitons- bound electron-hole pairs formed via Coulomb attraction after optical excitation. Unlike many magnetic materials, CrSBr exhibits a direct band gap of approximately 1.5 eV at the Γ point, where the wave vector $k = 0$ (**Figure 10**)[26]. This band gap underpins the semiconducting properties of CrSBr.

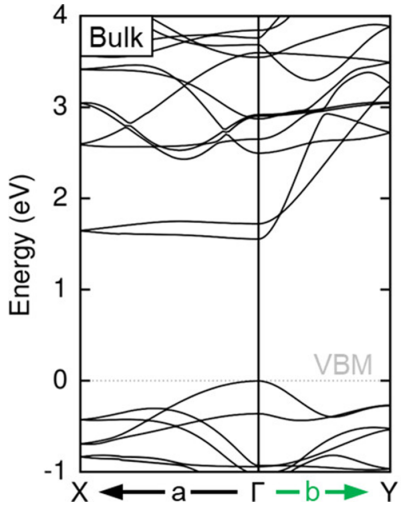

Figure 10: *Calculated electronic band structure for bulk CrSBr along the in-plane momentum directions in the antiferromagnetic ground state. Pronounced anisotropy is visible in the conduction band with a highly dispersive band in the* b *direction and an almost flat band in the* a *direction. This indicates high charge mobility along the* b *crystallographic axis. The direct band gap can be seen at the* Γ *point. Figure taken from Klein* et al.[26].

Ab-initio band structure calculations[9,26] reveal that the conduction band exhibits extreme anisotropy (**Figure 10**), appearing nearly flat along the $\Gamma - X$ direction (equivalent to the crystallographic a-axis) and highly dispersive along $\Gamma - Y$ direction (b-axis)[27]. As the conduction band possesses substantial orbital character from both Cr 3d ($\sim$ 60%) and S 3p ($\sim$ 40%) orbitals and Cr-S linkages extend along both the a- and b-axes (**Figure 1 (a)**), the origin of this difference is not immediately obvious. However, a single ion crystal field perspective for the Cr site shows that the local coordination sphere for each trivalent chromium ion is a CrS_4Br_2 distorted octahedron, lifting the degeneracy of the d orbitals and causing the corresponding d-orbital splitting seen in **Figure 11 (a)** and **(b)**. The conduction band is then derived from d_{z^2}- like orbitals and S 3p orbitals that form quasi-1D Cr-S chains propagating along the b-axis and overlap much more weakly along the a-axis.

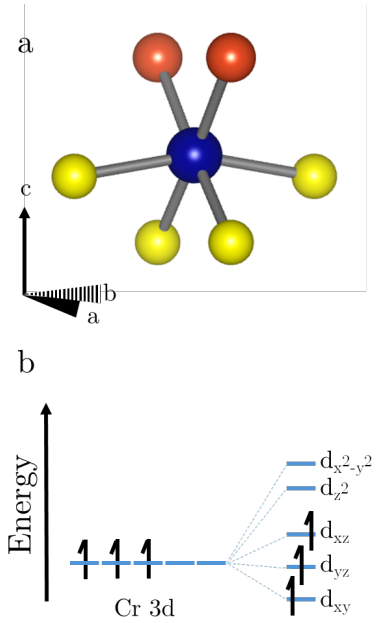

Figure 11: *Distorted octahedral coordination environment for a single Cr^{3+} ion in CrSBr and the corresponding d-orbital splitting. The crystallographic b-axis is used as the orbital z-axis. Figure adapted from Ziebel* et al. *[10]*

Photoluminescence (PL) spectroscopy provides a direct probe of these electronic and excitonic properties. Optical excitation promotes electrons across the band gap into the conduction band, leaving holes in the valence band. Subsequent relaxation and recombination processes emit photons with characteristic energies, which are detected by a spectrograph and camera. In CrSBr, the dominant excitonic transition appears in the near-infrared range (1.2-1.4 eV), consistently observed across a variety of experimental conditions and sample thicknesses[4,9,22,28]. It is therefore a useful indicator for characterising samples[26].

The intrinsic electronic anisotropy also manifests directly in optical response: the photoluminescence emmission is strongly polarised along the *b* crystallographic axis, a property enhanced by the fact that spins are oriented along the *b*-axis in the antiferromagnetic ground state[10].

2.3.1 Room Temperature Photoluminescence Spectroscopy

The characteristic dominant excitonic transition was observed at room temperature (298 K) using an excitation laser at 532 nm irradiating an exfoliated multilayer sample of CrSBr on a fused quartz glass slide. The position of this peak was found to be at 1.315(7) eV, which is in good agreement with values found in the literature[4,9,22,28]. The photoluminescence (PL) peak measured contained a Fabry-Pérot-like modulation that was caused by etalons resonance effects in the detector and so it was removed from data through use of a low pass Fourier Fast Transform (FFT) filter at 0.015 Hz. An example

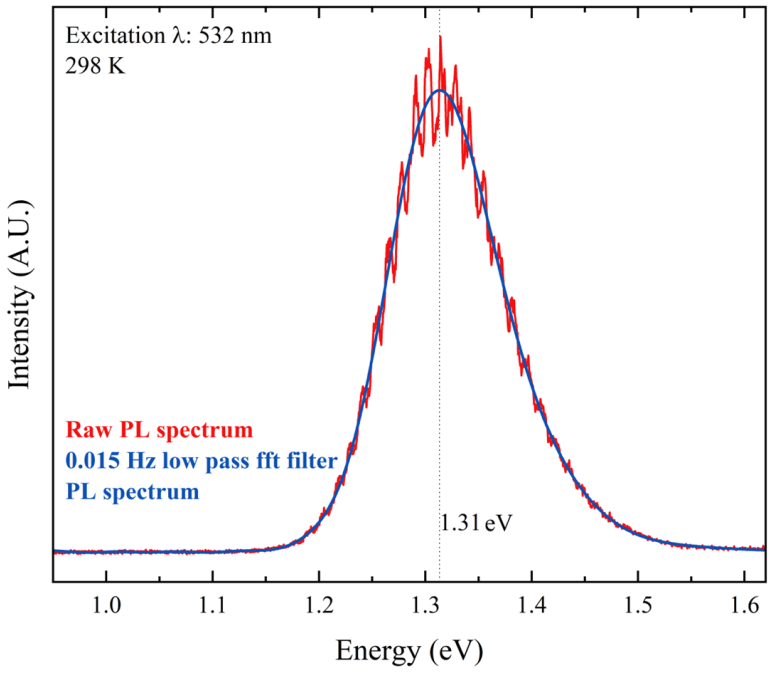

Figure 12: *Example photoluminescence emission spectrum of a multilayer exfoliated flake of CrSBr at 298 K, excited by a 532 nm laser and a power of approximately 100 μW. A single clear peak (red) is visible at 1.31 eV with an overlaying Fabry-Perot-like oscillation caused by interference effects in the optical components of the set-up. The feature can be easily removed with a 0.015 Hz low pass Fast Fourier Transform filter (shown in blue).*

photoluminescence spectrum is shown in **Figure 12** and depicts a clear peak with a full width half maximum (FWHM) of 0.12(3) eV.

As mentioned, the photoluminescence emission intensity is strongly polarised along the *b*-axis of the crystal. **Figure 13** illustrates this anisotropy, measured by rotating a linear grid polariser in the analyser position. The polariser angle was then calibrated with the crystallographic axes. This inherent emission polarisation was important to keep in mind in subsequent measurements.

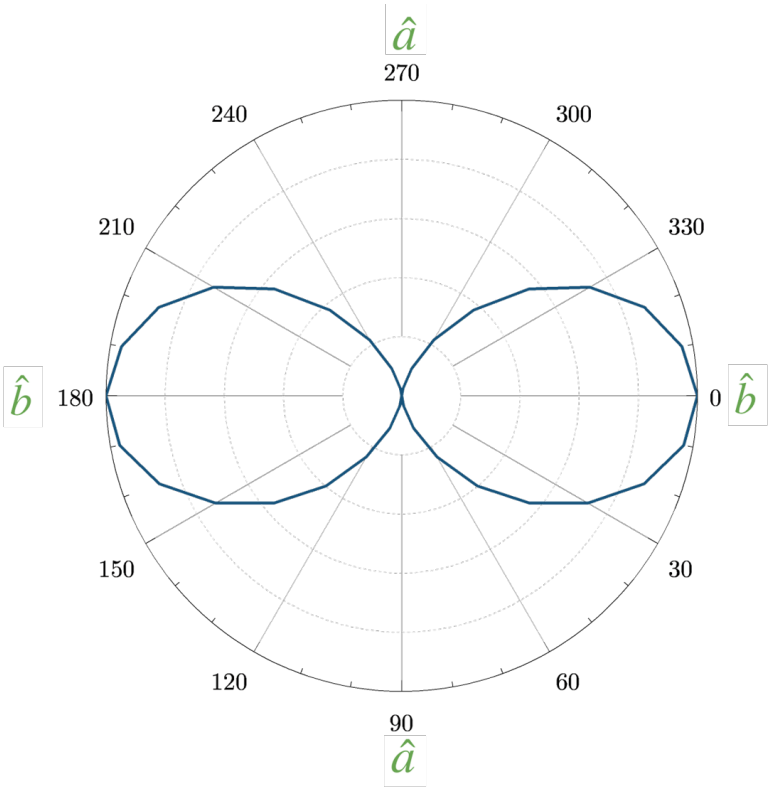

Figure 13: *Photoluminescence intensity as a function of analyser angle, demonstrating strong polarisation of the emission along the b-axis. The analyser (a linear polariser) was rotated by an angle indicated by the axis labels in the polar plot, and spectra were measured and integrated to determine the total area under each peak. Data is normalised to highlight the pronounced polarisation long the* b *direction. The green* $\hat{a}$ *and* $\hat{b}$ *labels indicate the crystallographic unit vector directions relative to the analyser angle.*

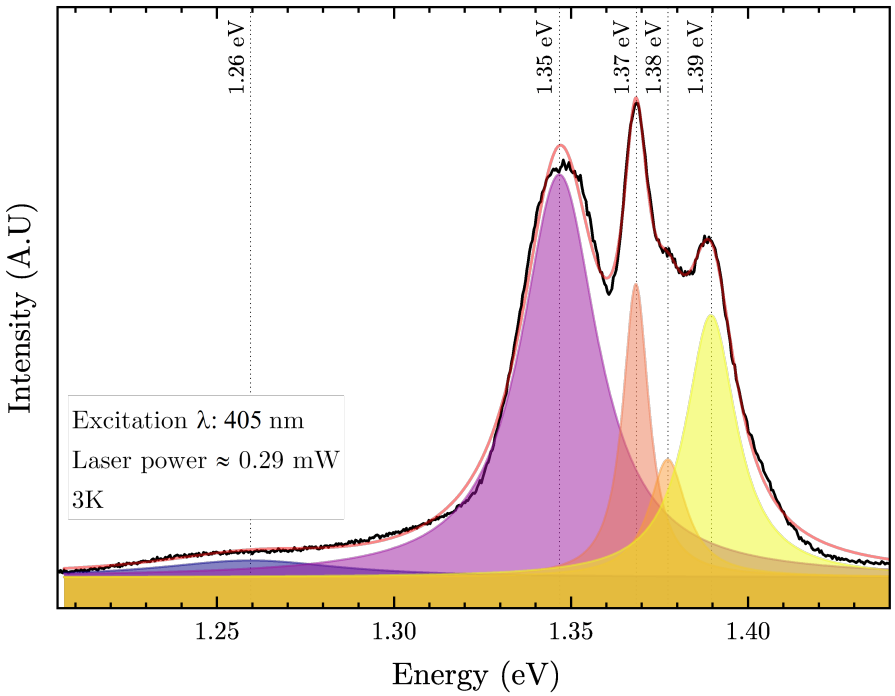

Figure 14: *Low temperature (3K) photoluminescence spectrum of a multilayer exfoliated flake of CrSBr under 405 nm excitation (0.29 mW), showing multiple emission features in the 1.2-1.4 eV range. The measured spectrum (black) is well reproduced by a multi-peak fit (pink), with individual Lorentzian components.*

2.3.2 Temperature-Dependent Photoluminescence Spectroscopy

In order to investigate the impact of the antiferromagnetic ordering on the photoluminescence spectrum of CrSBr, temperature resolved photoluminescence spectra were measured. The photoluminescence spectrum of CrSBr at 3 K under 405 nm excitation is plotted in **Figure 14** and exhibits a structured emission band in the 1.2-1.4 eV range from which several separate peaks can be resolved. As shown in **Figure 14**, the measured spectrum is well reproduced by a multi-component Lorentzian fit, revealing 5 distinct contributions. A weaker feature is seen around 1.26 eV, followed by the most dominant peak at 1.35 eV and then 3 weaker higher-energy features at 1.37, 1.38 and 1.39 eV. The weakest structure at 1.26 eV may be attributed to defect-related exciton recombination (known to become more visible at lower temperature), based on its lower energy, broad linewidth, and weak intensity. The two main peaks at 1.35 and 1.37 eV lie in the energy range widely reported for the 1s exciton in CrSBr (~ 1.35-1.37 eV)[26] and will hence be referred to as the main doublet (justified by the results shown later in **Figure 16**). The features observed above 1.37 eV may be attributed to higher energy excitonic states or fine structure, potentially arising from excited excitonic levels. Wilson et al[9] suggest that the asymmetric dielectric environment caused by the substrate may also brighten otherwise forbidden optical transitions, for example, involving the second conduction band roughly 40 meV higher in energy, ehich may explain these higher energy peaks. These features diminish with increasing temperature (**Figure 15**), consistent

with their weaker binding and increased susceptibility to thermal broadening.

The evolution of the photoluminescence spectra with temperature (3-295 K), shown in **Figure 15**, reveals several key trends. At low temperature, the emission consists of multiple well-resolved peaks, indicating discrete excitonic states at low temperature. As the temperature increases, these features progressively broaden and merge, accompanied by a reduction in overall intensity. The linewidth broadening with increasing temperature is characteristic of exciton-phonon interactions: increased lattice vibrations enhance scattering processes and reduce the coherence of the excitonic states. Concurrently, a slight redshift of the emission is observed, consistent with the expected reduction in the bandgap with increasing temperatures seen in semiconductors due to lattice expansion and electron-phonon coupling. A pronounced reduction in overall photoluminescence intensity is also observed at elevated temperature. This behaviour may be due to thermal quenching as non-radiative recombination pathways are enhanced via phonon-mediated scattering at higher temperatures, allowing excitons to relax via phonon emission or defect-assisted processes rather than radiative recombination.

A clearer picture of the temperature-dependent evolution is provided by the photoluminescence intensity heatmap in **Figure 16**. At low temperatures, two distinct excitonic peaks are clearly resolved. As the temperature increases, these peaks gradually merge into a single emission feature around ~ 130-140 K. This temperature range coincides with the known antiferromagnetic-to-paramagnetic phase transition (Néel temperature, T_N) seen in **Figure 5**. The behaviour seen in **Figure 16** is consistent with reports by Watson et al.[29], who observe a splitting of the electronic structure in angle-resolved photoemission spectroscopy (ARPES) that disappears above the Néel temperature which they attribute to giant exchange splitting (an energy difference between spin-up and spin-down states) caused by the magnetic ordering in the antiferromagnetic ground state. The splitting of the excitonic peak in photoluminescence measurements is also seen by Wilson et al.[9] and provides compelling evidence for the coupling between optical and magnetic properties in CrSBr. Below T_N, the presence of long-range magnetic order generates an effective exchange field that lifts the degeneracy of the excitonic state, resulting in two distinct energy states. Above T_N, the loss of magnetic order leads to the disappearance of this exchange field, and the excitonic emission collapses into a single peak. The observed energy splitting of approximately 10-20 meV is consistent with the expected scale of exchange interactions in this material, the exciton energy changes by approximately 20 meV when the system is forced into a field-polarised ferromagnetic state from the antiferromagnetic ground state[9]. Therefore, the results in **Figure 16** highlight a direct optical signature of the magnetic phase transition in CrSBr.

Important to note is the difference in the room temperature spectra as observed in in **Figures 15** and **12** with the photoluminescence spectrum using the 532 nm laser showing just one resolved peak and the spectrum using a 405 nm laser showing a more complicated structure. While measured on different

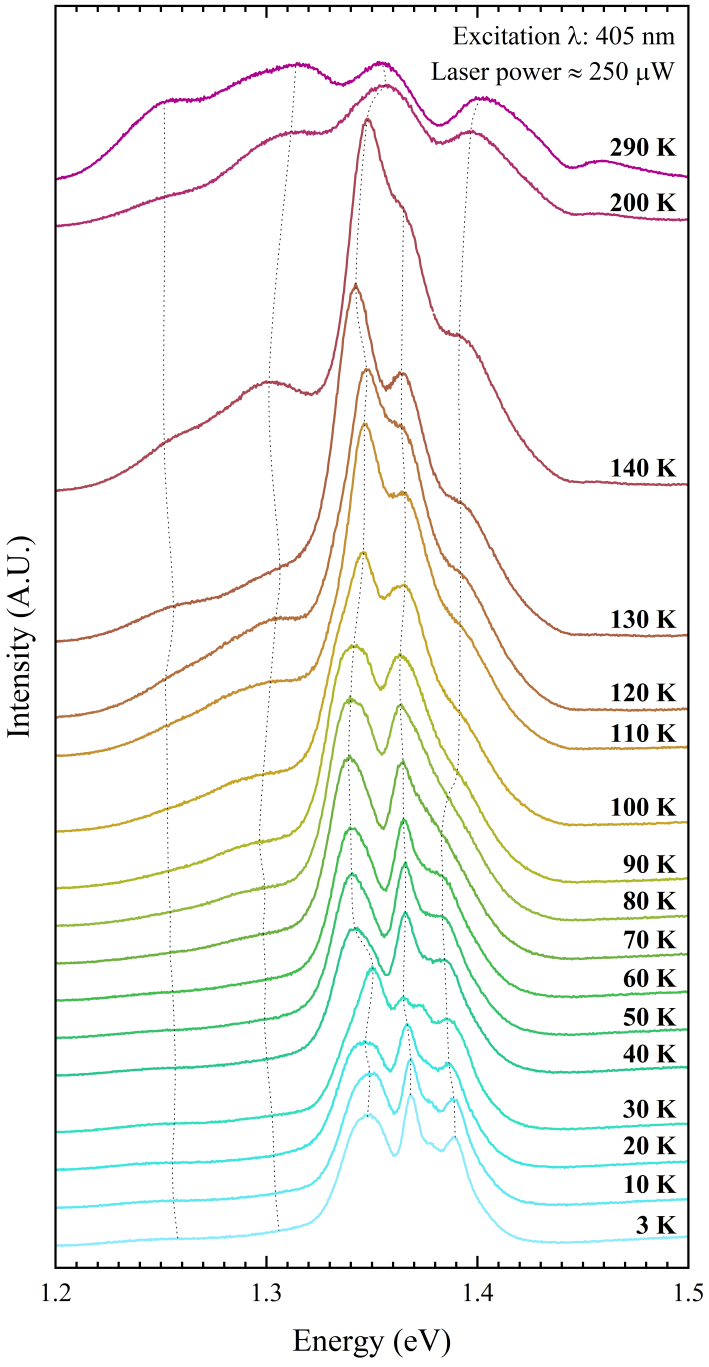

Figure 15: *Evolution of the photoluminescence spectra with increasing temperature (3-290 K) using a 405 nm excitation laser set to a power of approximately 250 μW. At low temperatures, well-resolved peaks are observed, which progressively broaden and merge with increasing temperature due to enhanced exciton-phonon interactions and thermal delocalisation. The data is normalised to the global maximum intensity.*

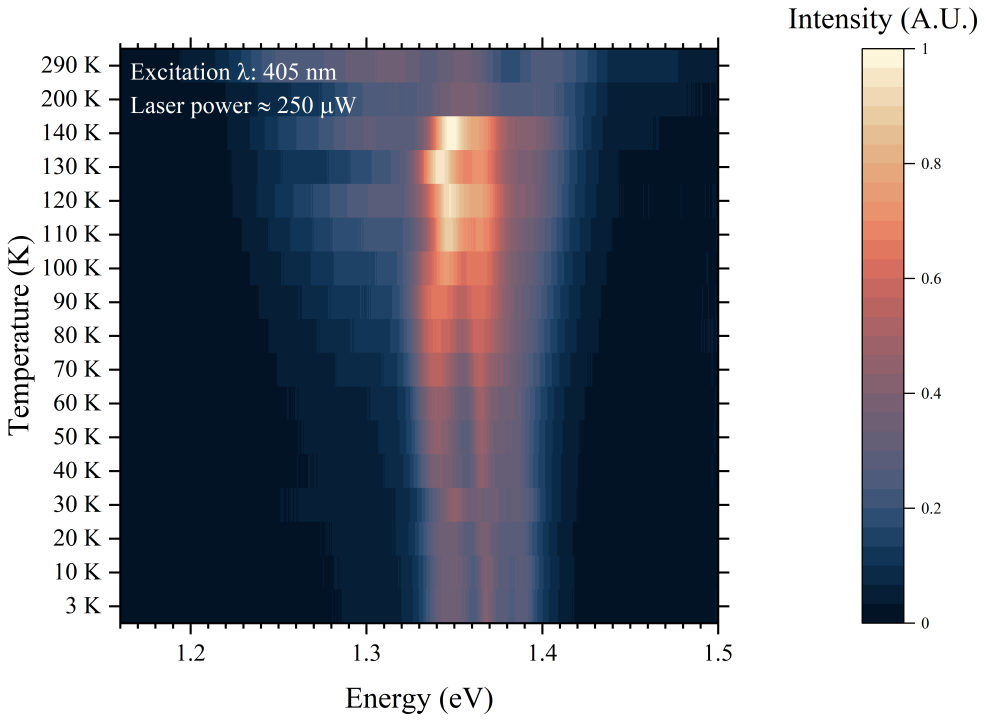

Figure 16: *Intensity heatmap of photoluminescence as a function of energy and temperature, normalised to the global maximum. Two distinct excitonic peaks are observed at low temperature, which merge into a single broad feature around 130-140 K, coinciding with the antiferromagnetic-to-paramagnetic phase transition. The overall photoluminescence intensity decreases with increasing temperature. The measurements were taken with an excitation laser at 405 nm set to a power of approximately 250 μW.*

setups, the difference in photoluminescence spectra remains unexpected (see **Figure 17** for a direct comparison). Further investigations are required to assess whether use of the same laser in the same set-up reproduces these results and failing that it would be interesting to see the wavelength dependence of the photoluminescence spectra at room temperature.

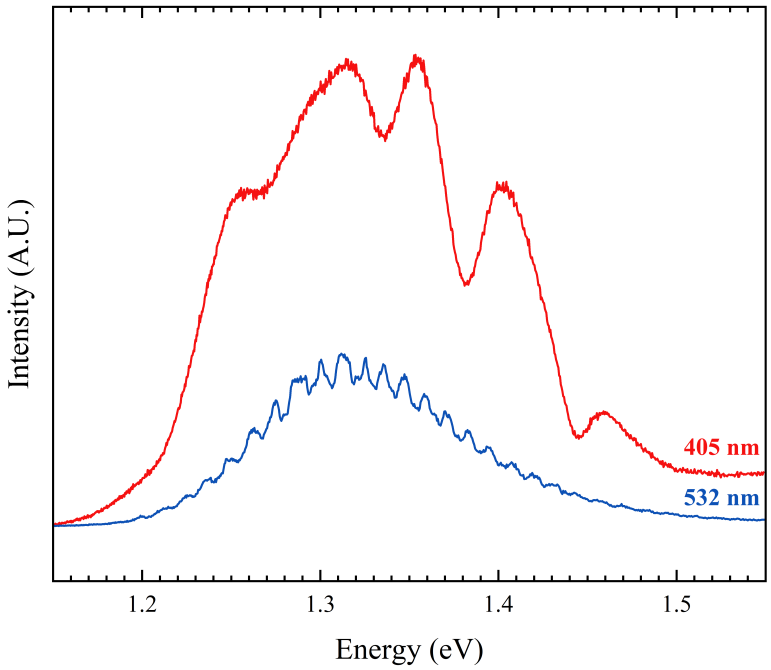

Figure 17: *A comparison of the photoluminescence peak seen at room temperature in two separate set-ups with two different excitation wavelengths, with intensity normalised to the global maximum. The spectra at 405 nm appears to have a more details sub structure than that measured at 532 nm.*

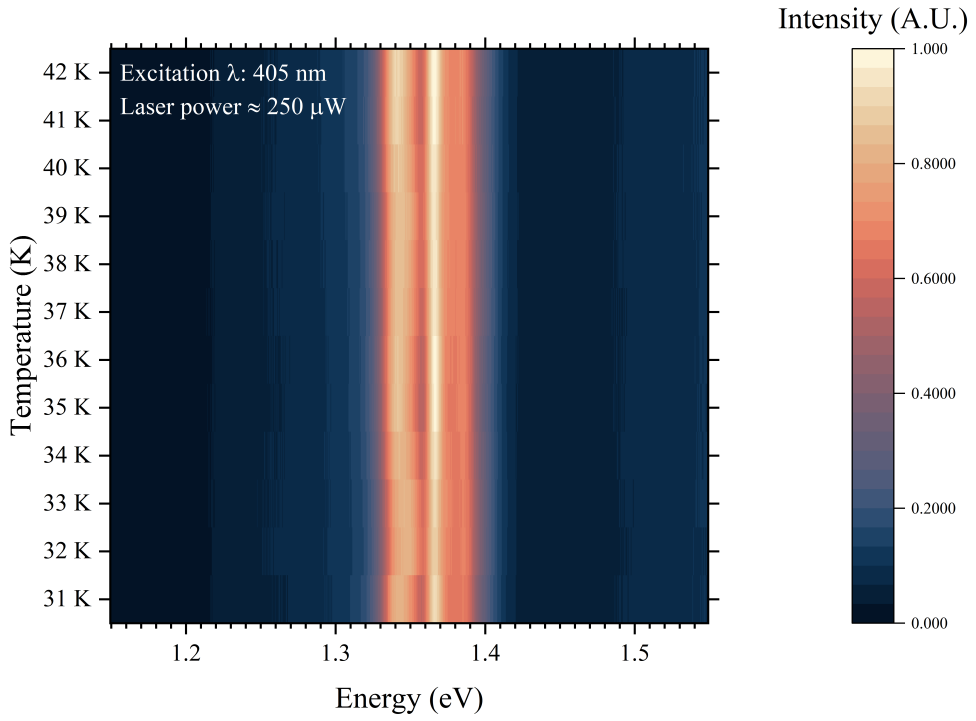

Figure 18: *Intensity map of photoluminescence as a function of energy and temperature near the temperature at which a low temperature feature was seen in magnetometry experiments. Two distinct excitonic peaks are observed which do not shift or change with increasing temperature. The measurements were taken with an excitation laser at 405 nm set to a power of approximately 250 μW. Data is normalised to the global maximum.*

2.3.3 Examining the Photoluminescence Spectra in the Low Temperature Magnetic Feature Temperature Range

A unique feature of CrSBr as a material is that it hosts strong coupling between its magnetic and electronic structures, which affects the optical and electronic properties during the field-induced antiferromagnetic-to-ferromagnetic transition[10]. To this end, it was interesting to see whether there was any change in the photoluminescence spectra across the temperature range where magnetometry measurements show the secondary peak at 39 K. **Figure 18** shows that when solely changing the temperature, the photoluminescence spectrum does not show significant changes around this low temperature feature, the peak position, shape and intensity are fairly constant. This is expected as the low temperature feature was only seen when an alternate magnetic field was applied. For this reason, further experiments will look at simulating the same AC magnetic field conditions as seen in the AC magnetic susceptibility measurements whilst measuring the photoluminescence spectra in a similar temperature range.

3 Conclusions and Future Outlook

Magnetometry and photoluminescence were successfully used to characterise the commercially produced CrSBr sample. The characteristic triaxial magnetic anisotropy of CrSBr was observed and it was possible to assign the easy, intermediate and hard magnetic axes to the crystallographic axes. The spin-flip transition and the gradual spin reorientations visible in the field induced transition from antiferromagnetic to ferromagnetic states were observed and in all cases, the saturation moment came close to the expected moment from 3 unpaired polarised spins. The samples studied showed the characteristic transition from paramagnetic to antiferromagnetic at 132.7(6) K and Curie-Weiss analysis of the paramagnetic regime is consistent with similar analysis seen in literature[8] and indicated that ferromagnetic correlations persist above the Néel temperature. This is an observation corroborated by Scheie et al[18] who show through single crystal neutron diffraction that these correlations exist in the *ab* plane.

Surprisingly, alongside the well-understood antiferromagnetic to paramagnetic transition at 132 K[8,9,12,18,19,21–23], a smaller feature at 39 K was observed in both AC and DC magnetic susceptibility measurements. A peak in the imaginary magnetic susceptibility extracted from AC measurements indicated that the feature is dissipative and splitting between the zero field cooled and field cooled DC magnetic susceptibility indicates that the feature may come from a ferromagnetic-like phase or frustrated exchange interactions that co-exist within the long range antiferromagnetic ordering. However, the observations in this study show some inconsistencies dependent on crystallographic orientation so repeat measurements are necessary to see if the results are reproducible. While this feature is previously reported in literature[8,12,13], it's dependence on field strength and frequency remained unexplored. The results in this work indicate that DC fields greater than 25 mT largely suppress the peak when measuring the AC magnetic susceptibility, which is likely the reason why the peak was much less noticeable in DC measurements made at 50 mT. The feature also displayed sensitivity to the frequency of the AC field, with increasing frequency suppressing and shifting the peak in the real part of the magnetic susceptibility. These results are consistent with dynamic behaviour, possibly indicative of a spin glass system that freezes at 39 K.

Photoluminescence measurements at room temperature with a 532 nm laser showed the characteristic lowest-energy exciton peak at 1.31 eV and it was shown that the photoluminescence emission was indeed strongly polarised along the *b*-axis. Temperature dependent photoluminescence showed the emergence of a composite peak, chiefly a doublet that merged into a singlet near the antiferromagnetic to paramagnetic transition temperature. This provides an optical signature of the transition and confirms that the magnetic structure influences the optical landscape in CrSBr. To this end, the photoluminescence spectra were carefully studied at temperatures near 39 K, to see if the feature seen in AC magnetic

susceptibility measurements would affect 0-field photoluminescence measurements. No change was observed as is expected as the feature only emerged under an AC magnetic field in magnetometry measurements.

Interestingly, the photoluminescence spectra at room temperature differed greatly between the cryogenic photoluminescence set-up with an excitation wavelength of 405 nm and the ambient photoluminescence set-up with an excitation wavelength of 532 nm. This may be due to an inherent wavelength dependence of the photoluminescence spectra, or most likely an extrinsic effect due to differences in the experimental set-ups. Further investigation is necessary to understand this.

Overall, the research outlined in this report successfully characterises the CrSBr crystals studied and illuminates new properties regarding the low temperature magnetic phase diagram of CrSBr. This is essential for further study and integration into metasurfaces. The research presented in this work raises several important questions that warrant further investigation. Of high priority is establishing the reproducibility of the observed results across multiple samples, particularly given the sensitivity of magnetic and optical properties to sample quality in layered materials.

A key unresolved issue is the significant variation observed in the room-temperature photoluminescence spectra between experimental set-ups. Systematic investigation of excitation wavelength dependence of the photoluminescence response would help determine whether this discrepancy arises from intrinsic material behaviour or extrinsic experimental factors. In addition, studying the power dependence of the photoluminescence response would provide further insight into excitonic processes and facilitate more reliable comparisons between datasets. Further work is also required to establish robust correlations between optical contrast and sample thickness, and layer number in CrSBr. Such calibration would enable more accurate characterisation of exfoliated samples and improve reproducibility across experiments.

On the magnetic side, improved DC magnetic susceptibility measurements at lower applied fields and across a larger set of samples are necessary to more clearly resolve the splitting between zero field cooled and field cooled measurements. This may be aided by preparing larger samples to enhance signal quality and reduce measurement uncertainty. Ultimately, measurements would be improved by performing them with a SQUID magnetometer- a more sensitive technique.

Finally, a particularly promising direction is to directly probe the coupling between magnetic and optical behaviour around the low-temperature feature near 39 K. This could be achieved by performing temperature-dependent photoluminescence measurements under an applied AC magnetic field with comparable amplitude and frequency to those used in magnetometry. Implementation of such measurements, for example via a simple coil system integrated into the cryogenic photoluminescence set-up,

would allow direct investigation of whether the magnetic dynamics responsible for this feature influence the optical response, as observed for field-induced magnetic transitions in $CrSBr$[9].

4 Methodology

4.1 Magnetometry Measurements

DC magnetometry and AC susceptibility measurements were made with the Quantum Design PPMS DynaCool system equipped with the ACMS II option. A single CrSBr crystal (1.9 mg) was carefully cut to the right size for mounting by using micro tools. The crystal was mounted to a quartz paddle for the *a*- and *b*- crystallographic axes and to quartz braces fixed in a brass paddle for the *c*-axis. In each case, the crystallographic axis being studied was oriented parallel to the length of the paddle. The crystal was attached using GE varnish cured at room temperature for a minimum of 1 hour. The same crystal was used for all axial-orientated measurements and the variable temperature scans and field-dependent magnetic susceptibility curves for each axis were measured during the same measurement cycle. The crystal was removed using isopropanol, dried in air and then reorientated and reattached as described previously.

Unfortunately, due to the ease with which CrSBr exfoliates, some sample was lost in the removing stages. Estimates of mass lost were made by comparison of saturation moments and it was estimated that the mass reduced to 1.887 mg between mounting the *b*- and *a*-axes and further to 1.642 mg between mounting the *a* and *c*-axes. The loss of mass may be reduced by mounting the crystal within tape before reattaching the tape and crystal to the paddles with GE varnish as usual- the crystal would remain within the tape package. The tape mass could be recorded and its diamagnetic response could then be taken into account during data analysis.

4.2 Flake Exfoliation

Thin, multilayer CrSBr flakes were prepared from commercially obtained (HQ Graphene) CrSBr crystals via mechanical exfoliation with Nitto SPV-244 tape. The exfoliated samples were then transferred onto fuzed quartz (SiO_2) by use of Gel-Pak WF-30 polydimethylsiloxane (PDMS). All flake preparation was performed in a home-built box with nitrogen flow that lowered humidity to 30% to increase success of exfoliations. After a sample was prepared, it was stored in a dry argon glovebox until needed for measurements. Thickness of the exfoliated flakes could be estimated by optical contrast using LED light in the WITec alpha300 confocal Raman microscope. The long axis of the needle-like crystals was visually correlated to the *a* crystal axis.

4.3 Optical Spectroscopy at Room Temperature

Photoluminescence spectroscopy was carried out using the WITec alpha300 confocal Raman microscope. The sample was mounted on a capacitively controlled piezo stage with 3 nm lateral positioning accuracy and excited with a fibre coupled continuous wave laser with an off-resonance excitation wavelength of 532 nm focused by a Zeiss EC Epiplan-Neofluar 100 objective. The excitation polarisation axis was set along the b-axis of the sample through use of a half wave plate and all polarisations of photoluminescence emission were collected by the same Zeiss objective, split by a fibre-coupled WITec UHTS 300 spectrometer (Blaze 500 nm and grating 150 g/mm) and detected by the Andor Newton EMCCD camera cooled to -60 ° C to suppress electronic noise. Measurements were made in ambient conditions using a laser power of approximately 200 μW.

4.4 Cryogenic Optical Spectroscopy

Temperature dependent photoluminescence spectroscopy measurements were conducted using a home-built set-up. The CrSBr sample on its fuzed quartz slide is mounted on a cold stage (using silver paint for thermal contact) in a Montana Instruments vertical cryo-optic sample chamber (s50-CO) connected to a closed-cycle helium Montana Instruments CryoAdvance50 cryostat which can be cooled down to 3 K. A 405 nm picosecond diode laser was used to excite the sample through Zeiss Epiplan-Neofluar 100x objective and the emitted light is chromatically dispersed by a Princeton Instruments SpectraPro 2300i Spectrometer (Blaze 500 nm and grating 150 g/mm) onto a Pixis Si CCD camera (cooled to -70 °C). An on-sample power of approximately 250 μW was used throughout measurements and a halfwaveplate was used to ensure excitation polarisation was aligned with the crystallographic b direction.

References

[1] K. S. Burch, D. Mandrus and J.-G. Park, *Nature*, 2018, **563**, 47–52.

[2] K. S. Novoselov, A. K. Geim, S. V. Morozov, D. Jiang, Y. Zhang, S. V. Dubonos, I. V. Grigorieva and A. A. Firsov, *Science*, 2004, **306**, 666–669.

[3] A. M. Shaltout, A. V. Kildishev and V. M. Shalaev, *Journal of the Optical Society of America B*, 2016, **33**, 501.

[4] A. K. Demir, L. Nessi, S. Vaidya, C. A. Occhialini, M. Soljačić and R. Comin, *Nature Photonics*, 2025, **19**, 1006–1012.

[5] J. Cenker, S. Sivakumar, K. Xie, A. Miller, P. Thijssen, Z. Liu, A. Dismukes, J. Fonseca, E. Anderson, X. Zhu, X. Roy, D. Xiao, J.-H. Chu, T. Cao and X. Xu, *Nature Nanotechnology*, 2022, **17**, 256–261.

[6] K. Bagani, A. Vervelaki, D. Jetter, A. Devarakonda, M. A. Tschudin, B. Gross, D. G. Chica, D. A. Broadway, C. R. Dean, X. Roy, P. Maletinsky and M. Poggio, *Nano Letters*, 2024, **24**, 13068–13074.

[7] F. Tabataba-Vakili, H. P. G. Nguyen, A. Rupp, K. Mosina, A. Papavasileiou, K. Watanabe, T. Taniguchi, P. Maletinsky, M. M. Glazov, Z. Sofer, A. S. Baimuratov and A. Högele, *Nature Communications*, 2024, **15**, 4735.

[8] E. J. Telford, A. H. Dismukes, R. L. Dudley, R. A. Wiscons, K. Lee, D. G. Chica, M. E. Ziebel, M.-G. Han, J. Yu, S. Shabani, A. Scheie, K. Watanabe, T. Taniguchi, D. Xiao, Y. Zhu, A. N. Pasupathy, C. Nuckolls, X. Zhu, C. R. Dean and X. Roy, *Nature Materials*, 2022, **21**, 754–760.

[9] N. P. Wilson, K. Lee, J. Cenker, K. Xie, A. H. Dismukes, E. J. Telford, J. Fonseca, S. Sivakumar, C. Dean, T. Cao, X. Roy, X. Xu and X. Zhu, *Nature Materials*, 2021, **20**, 1657–1662.

[10] M. E. Ziebel, M. L. Feuer, J. Cox, X. Zhu, C. R. Dean and X. Roy, *Nano Letters*, 2024, **24**, 4319–4329.

[11] K. Yang, G. Wang, L. Liu, D. Lu and H. Wu, *Physical Review B*, 2021, **104**, 144416.

[12] S. A. López-Paz, Z. Guguchia, V. Y. Pomjakushin, C. Witteveen, A. Cervellino, H. Luetkens, N. Casati, A. F. Morpurgo and F. O. Von Rohr, *Nature Communications*, 2022, **13**, 4745.

[13] J. Klein, Z. Song, B. Pingault, F. Dirnberger, H. Chi, J. B. Curtis, R. Dana, R. Bushati, J. Quan, L. Dekanovsky, Z. Sofer, A. Alù, V. M. Menon, J. S. Moodera, M. Lončar, P. Narang and F. M. Ross, *ACS Nano*, 2023, **17**, 288–299.

[14] S. W. Song, J. Klein, K. Mosina, Z. Sofer, D. Sedmidubský, J. Dong, K. Chen, F. M. Ross and R. Jaramillo, *The Journal of Physical Chemistry C*, 2025, **129**, 19002–19011.

[15] F. Long, K. Mosina, R. Hübner, Z. Sofer, J. Klein, S. Prucnal, M. Helm, F. Dirnberger and S. Zhou, *Applied Physics Letters*, 2023, **123**, 222401.

[16] J. Beck, *Zeitschrift für anorganische und allgemeine Chemie*, 1990, **585**, 157–167.

[17] J. Kanamori, *Journal of Physics and Chemistry of Solids*, 1959, **10**, 87–98.

[18] A. Scheie, M. Ziebel, D. G. Chica, Y. J. Bae, X. Wang, A. I. Kolesnikov, X. Zhu and X. Roy, *Advanced Science*, 2022, **9**, 2202467.

[19] O. Göser, W. Paul and H. Kahle, *Journal of Magnetism and Magnetic Materials*, 1990, 129–136.

[20] E. J. Telford, D. G. Chica, M. E. Ziebel, K. Xie, N. S. Manganaro, C. Huang, J. Cox, A. H. Dismukes, X. Zhu, J. P. S. Walsh, T. Cao, C. R. Dean and X. Roy, *Advanced Physics Research*, 2023, **2**, 2300036.

[21] K. Lee, A. H. Dismukes, E. J. Telford, R. A. Wiscons, J. Wang, X. Xu, C. Nuckolls, C. R. Dean, X. Roy and X. Zhu, *Nano Letters*, 2021, **21**, 3511–3517.

[22] E. J. Telford, A. H. Dismukes, K. Lee, M. Cheng, A. Wieteska, A. K. Bartholomew, Y. Chen, X. Xu, A. N. Pasupathy, X. Zhu, C. R. Dean and X. Roy, *Advanced Materials*, 2020, **32**, 2003240.

[23] T. M. J. Cham, S. Karimeddiny, A. H. Dismukes, X. Roy, D. C. Ralph and Y. K. Luo, *Nano Letters*, 2022, **22**, 6716–6723.

[24] C. Boix-Constant, S. Mañas-Valero, A. M. Ruiz, A. Rybakov, K. A. Konieczny, S. Pillet, J. J. Baldoví and E. Coronado, *Advanced Materials*, 2022, **34**, 2204940.

[25] J. Klein, T. Pham, J. D. Thomsen, J. B. Curtis, T. Denneulin, M. Lorke, M. Florian, A. Steinhoff, R. A. Wiscons, J. Luxa, Z. Sofer, F. Jahnke, P. Narang and F. M. Ross, *Nature Communications*, 2022, **13**, 5420.

[26] J. Klein, B. Pingault, M. Florian, M.-C. Heißenbüttel, A. Steinhoff, Z. Song, K. Torres, F. Dirnberger, J. B. Curtis, M. Weile, A. Penn, T. Deilmann, R. Dana, R. Bushati, J. Quan, J. Luxa, Z. Sofer, A. Alù, V. M. Menon, U. Wurstbauer, M. Rohlfing, P. Narang, M. Lončar and F. M. Ross, *ACS Nano*, 2023, **17**, 5316–5328.

[27] F. Wu, I. Gutiérrez-Lezama, S. A. Lopéz-Paz, M. Gibertini, K. Watanabe, T. Taniguchi, F. O. v. Rohr, N. Ubrig and A. F. Morpurgo, *Advanced Materials*, 2022, **34**, 2109759.

[28] F. Dirnberger, J. Quan, R. Bushati, G. M. Diederich, M. Florian, J. Klein, K. Mosina, Z. Sofer, X. Xu, A. Kamra, F. J. García-Vidal, A. Alù and V. M. Menon, *Nature*, 2023, **620**, 533–537.

[29] M. D. Watson, S. Acharya, J. E. Nunn, L. Nagireddy, D. Pashov, M. Rösner, M. Van Schilfgaarde, N. R. Wilson and C. Cacho, *npj 2D Materials and Applications*, 2024, **8**, 54.

9516 words 50718 characters (not including spaces)

```
File: main.tex
Encoding: utf8
Sum count: 8638
Words in text: 7260
Words in headers: 91
Words outside text (captions, etc.): 1203
Number of headers: 25
Number of floats/tables/figures: 20
Number of math inlines: 83
Number of math displayed: 1
Subcounts:
  text+headers+captions (#headers/#floats/#inlines/#displayed)
  30+1+0 (1/0/0/0) Section: Confidentiality
  39+1+0 (1/0/0/0) Section: Declaration
  586+1+0 (1/0/0/0) Section: Acknowledgements
  267+1+0 (1/0/0/0) Section: Abstract
  30+1+0 (1/0/0/0) Section: Abbreviations
  594+4+0 (1/0/0/0) Section: Project Background and Objectives} \label{background
  304+4+0 (1/0/0/0) Subsection: Project Aims and Objectives
  0+3+0 (1/0/0/0) Section: Results and Discussion
  379+11+166 (3/4/24/0) Subsection: Background Theory and Information
  2034+26+513 (4/7/31/1) Subsection: Magnetic Characterisation
  1475+21+524 (4/9/23/0) Subsection: Optical Characterisation
  886+4+0 (1/0/0/0) Section: Conclusions and Future Outlook
  0+1+0 (1/0/0/0) Section: Methodology
  260+2+0 (1/0/0/0) Subsection: Magnetometry Measurements
  112+2+0 (1/0/1/0) Subsection: Flake Exfoliation
  131+5+0 (1/0/2/0) Subsection: Optical Spectroscopy at Room Temperature
  133+3+0 (1/0/2/0) Subsection: Cryogenic Optical Spectroscopy

File: output.bbl
Encoding: utf8
Sum count: 878
Words in text: 878
```

```
Words in headers: 0
Words outside text (captions, etc.): 0
Number of headers: 0
Number of floats/tables/figures: 0
Number of math inlines: 0
Number of math displayed: 0

Total
Sum count: 9516
Words in text: 8138
Words in headers: 91
Words outside text (captions, etc.): 1203
Number of headers: 25
Number of floats/tables/figures: 20
Number of math inlines: 83
Number of math displayed: 1
Files: 2
Subcounts:
  text+headers+captions (#headers/#floats/#inlines/#displayed)
  7260+91+1203 (25/20/83/1) File(s) total: main.tex
  878+0+0 (0/0/0/0) File(s) total: output.bbl
```